Laboratory simulation of martensite formation of white etching layer in rail steel

Wu, Jun; Petrov, Roumen H.; Naeimi, Meysam; Li, Zili; Dollevoet, Rolf; Sietsma, Jilt

DOI
10.1016/j.ijfatigue.2016.05.016

Publication date
2016

Document Version
Final published version

Published in
International Journal of Fatigue

International Journal of Fatigue 91 (2016) 11–20

Contents lists available at ScienceDirect

International Journal of Fatigue

journal homepage: www.elsevier.com/locate/ijfatigue

Laboratory simulation of martensite formation of white etching layer in rail steel

Jun Wu [a,b,*], Roumen H. Petrov [a,b], Meysam Naeimi [c], Zili Li [c], Rolf Dollevoet [c], Jilt Sietsma [a,b]

[a] Department of Materials Science and Engineering, Delft University of Technology, Mekelweg 2, 2628 CD Delft, The Netherlands
[b] Department of Materials Science and Engineering, Ghent University, Technologiepark 903, 9052 Ghent, Belgium
[c] Section of Railway Engineering, Faculty of Civil Engineering and Geosciences, Delft University of Technology, Stevinweg 1, 2628 CN Delft, The Netherlands

ARTICLE INFO

Article history:
Received 25 January 2016
Received in revised form 13 May 2016
Accepted 16 May 2016
Available online 18 May 2016

Keywords:
White etching layer
Martensite formation
Laboratory simulation
Temperature rise
Thermodynamic calculations

ABSTRACT

White etching layer (WEL) is a frequently observed microstructural phenomenon in rail surface, formed during dynamic wheel/rail contact. It is considered as one of the main initiators for rolling contact fatigue cracks. There are several hypotheses for the formation mechanism of WEL. However, due to the complicated wheel/rail contact conditions, none is directly proven. Currently, the most popular hypotheses refer to either formation of martensitic WEL by phase transformations or formation of nanocrystalline ferritic WEL by severe plastic deformation. In this work, WEL formation by martensitic transformation in R260Mn grade pearlitic rail steel was simulated by fast heating and quenching experiments. Microstructural characteristics of the simulated WEL and WEL observed in a field rail specimen were characterized by microhardness, optical microscopy, scanning electron microscopy and electron backscatter diffraction. Microstructures of the two WELs were compared and similarities in morphology were identified. Numerical simulation shows the possible temperature rise up to austenitizing temperatures. Combining comparisons of experimental simulation with observation of WEL in the rail and the thermodynamic calculations, the hypothesis for WEL formation via martensitic transformation is supported.

1. Introduction

Rolling contact fatigue (RCF) is the dominant damage mechanism in rails and has attracted wide scientific interest. The high and repetitive external load, exceeding 1 GPa, leads to formation of peculiar surface structural alterations, surface crack formation and spallation [1,2]. One such specific structural phenomenon in rail surface is widely named white etching layer (WEL) [1–7]. WEL is commonly recognized as a thin and hard layer, which appears white under light reflection after being etched in 2–5% HNO_3 in ethanol (Nital etchant). Widely accepted opinion is that the extremely high hardness of WEL, up to 1200 HV [6], is related to its brittleness. RCF cracks associated with WEL are frequently observed in rails [2].

The most popular hypotheses for WEL formation are: (i) martensite formed after the rail surface is heated up to austenitization temperatures and subsequently quenched, e.g. [5], and (ii) nanocrystalline ferrite as a result of severe plastic deformation [4]. A brief summary of the above two proposed mechanisms is given in Table. 1. There is experimental evidence for the WEL formation via martensite phase transformation. In synchrotron X-ray diffraction (XRD) experiments, the WEL is shown to consist of bcc iron and the tetragonal crystal lattice distortion is identified [5,8]. This is a typical feature for high carbon martensite. Detection of retained austenite [5,8] indicates martensitic nature of the WEL to be the most probable. Occasionally, the martensite type features, such as the lath morphology [7] and the micro-twinning substructure [5], are observed in WEL by means of transmission electron microscopy (TEM). Martensite with similar hardness as WEL in [5] can be simulated by laser heat treatment. Takahashi studied WEL in rails using combination of microhardness, scanning electron microscope (SEM) and atom probe tomography (APT) [7]. He claimed the absence of severe plastic deformation in the studied rail, from the observation of unchanged cementite interlamellar distance in the rail surface pearlite and the absence of work-hardened pearlite zone beneath the WEL. In addition, identification of manganese diffusion, from cementite to the ferrite lamellae in the WEL by means of APT, indicates a strong temperature rise caused by wheel/rail contact. This evidence tends to conclude that WEL is formed by martensitic phase transformation.

* Corresponding author at: Department of Materials Science and Engineering, Delft University of Technology, Mekelweg 2, 2628 CD Delft, The Netherlands.
E-mail address: jun.wu@tudelft.nl (J. Wu).

http://dx.doi.org/10.1016/j.ijfatigue.2016.05.016
0142-1123/

Table 1
Summary of the formation mechanisms of white etching layer.

Proposed mechanism	Supporting evidence
	Detection of tetragonality and retained austenite in WEL by synchrotron XRD [5,8] Martensite like morphology in WEL revealed by TEM, e.g. micro-twinning [5] or lath-like morphology [7]
WEL formed by martensitic transformation	Simulation of martensite with similar hardness as WEL by laser heating experiment [5]
	Absence of transient work-hardened pearlite zone below WEL by hardness measurements and no observation of cementite lamellae thinning from APT results [7] Manganese diffusion revealed by APT [7] Temperature calculation does not support martensite transformation mechanism for WEL formation in [9,10]
WEL formed by plastic deformation	Observation of deformation characteristics in WEL and the pearlite beneath WEL [9,10] Reproduction of WEL by severe plastic deformation [4,10] Similar thermal stability of the WEL and nanocrystalline ferrite formed by mechanical alloying, using DSC [4]

However, calculations of temperature rise caused by wheel/rail contact does not support the martensitic transformation for the WEL formation in [9,10]. Reaching the austenitizing temperature, e.g. 727 °C for the eutectoid steel, has been shown to be improbable. Instead, observations of possible deformation twinning in the WEL and the work-hardened pearlite zone below WEL have been made [9,10]. In addition, pearlite after severe plastic deformation is shown to resemble similar features as the WEL, such as cementite dissolution, nanometre grains and high hardness [4]. Differential Scanning Calorimetry (DSC) scans reveal a similar decomposing behaviour of the WEL and the pearlite after mechanical alloying [4], indicating a similar microstructure type. The extremely high dislocation density in the WEL is estimated to be able to accommodate the amount of carbon from the dissolved cementite. As a result, WEL formation due to plastic deformation is proposed [4,9,10].

In this study, WEL formation by martensitic transformation mechanism is simulated in laboratory conditions. The WEL formed by martensitic transformation must be a product of (ultra)fast phase transformation because of wheel/rail contact. According to [7], the heating rate generated during train passage can be higher than 10^6 °C/s to the temperature where austenite forms. After train passage, the austenite transforms to martensite during fast cooling. Due to the extremely short wheel/rail contact time, estimated to be milliseconds using the heating rate of 10^6 °C/s from room temperature to 727 °C for the eutectoid iron steel, it is almost impossible to measure the actual temperature changes during the period. On the other hand, fast heating and quenching heat treatment can be simulated and controlled using laboratory instruments, such as dilatometer and thermo-mechanical simulator. The latter instrument also provides accurate loading controls, such as (high) strain rate, which is more suitable to simulate the combined thermal and mechanical situation of wheel/rail contact. In this study, WEL formation by fast phase transformation mechanism is simulated by the thermo-mechanic simulator. The microstructural features are characterized and compared with WEL observed in rails. Similarity of the laboratory WEL and WEL in rails will be discussed on the basis of the current observations and comparison with the literature.

2. Materials and methods

R260Mn grade rail steel, cut from a straight rail track [11], was investigated. The steel has a composition of Fe–0.67 wt% C–1.51 wt % Mn–0.21 wt% Si, with a nearly fully pearlitic microstructure. The average pearlite colony size is 20 μm and the average cementite interlamellar distance is 150 nm. For WEL formation in laboratory conditions, cylindrical samples of ø6 mm × 75 mm were cut from the bottom of rail head, where the materials is considered to be free from plastic deformation from train passages. Thermocouples were welded in the specimen centre to measure the temperature changes during the experiments, Fig. 1(a).The samples were subjected to fast heating and quenching treatment by a Gleeble 1500 thermo-mechanical simulator. The specimens were quickly heated to temperatures between 730 °C and 930 °C, see Fig. 1(b). Heating rates of 20 °C/s and 200 °C/s were used to carry out the experiments. After heating to the selected temperature, the specimens were immediately quenched at a rate of 67 °C/s, using helium gas, to transform austenite to martensite. It will be shown that austenite forms after being heated to the designed temperatures.

In the following sections, the laboratory samples will be named '$S_{xxx-yyy}$', where letter S means the simulated sample and the first three symbols refer to the temperature samples are heated to xxx °C and the last three symbols are the heating rate, yyy °C/s. For example $S_{730-020}$ is the simulated specimen which is heated to 730 °C at the rate of 20 °C/s. Additionally, rail samples, containing WEL, were also studied and will be named 'rail WEL' through the rest of the paper.

The microstructures in both laboratory simulated samples and rail samples were characterized by microhardness tests, optical microscopy (OM) and scanning electron microscopy (SEM). After each heat treatment cycle, the specimens were cut transversely at the position where thermocouples were welded, see the inset in Fig. 1(a). The specimens for metallographic studies were prepared following the routine preparation procedure. A 2 vol% Nital etchant was used to reveal the microstructures. The microhardness was measured with a Durascan 70 (Struers) hardness tester, using a load of 1 N for 10 s. The microstructures were first characterized with an Olympus BX60 M optical microscope. The samples were further analyzed with a Jeol 6500F SEM.

Electron Backscatter Diffraction (EBSD) measurements were done on the rail specimen containing WEL. Specimen $S_{730-200}$ was also analyzed by EBSD for comparison. The sample preparation procedure reported in [11] was used in the study. The EBSD measurements were carried out in a FEI Quanta-450 SEM equipped with a field emission gun (FEG) and Hikari-Pro, EBSD detector. EDAX-TSL OIM Data Collections v.6.2 was used for data acquisition. All measurements were performed with accelerating voltage of 20 kV, FEI-spot size of 5 for 40 μm final aperture, step size of 50 nm and a hexagonal scan grid mode. With these settings ~90% of the orientation data points were correctly indexed with confidence index higher than 0.06. The orientation data were analyzed by means of TSL OIM Data analysis v. 7 without additional post-processing (cleaning) and the grains were defined as regions containing minimum 4 pixels with an internal misorientation more than 5°.

In order to provide thermodynamic basis for the design of heat treatments and for the interpretations of the obtained results, the equilibrium quasi-binary iron–carbon phase diagram was calculated by Thermo-Calc® Windows (TCW™), version S. According to Ref. [12], the peak normal pressure during wheel/rail contact in the new profile rail can reach up to 1.8 GPa, which affects the phase diagram [13]. In this work, the hydrostatic pressure of 1.8 GPa was used and its effect on the equilibrium phase diagram was evaluated using Thermo-Calc.

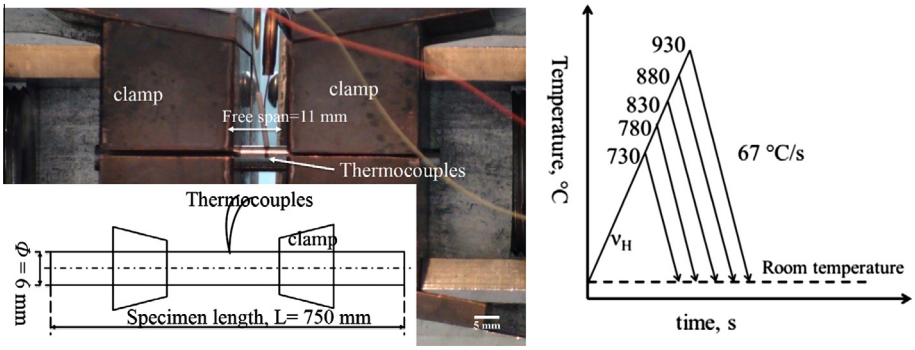

Fig. 1. (a) Configuration settings of Gleeble 1500 used in the laboratory simulations. The inset in the left bottom of the figure schematically shows the dimensions of the specimen and position of thermocouple. The two parallel arrows in the inset indicate the position where the specimen for microstructure characterization was cut after the heat treatment; (b) schematic representation of heat treatments used for WEL formation simulation in laboratory conditions.

3. Results

3.1. Iron-carbon phase calculations

The calculated equilibrium quasi-binary iron–carbon (Fe–C) phase diagram under atmospheric pressure is shown in Fig. 2(a) and the one calculated under hydrostatic pressure of 1.8 GPa is shown in Fig. 2(b). The vertical dashed lines in both figures indicate the carbon concentration of the studied rail steel of 0.67 wt%. In the equilibrium Fe–C phase diagram under atmospheric pressure for the present composition in Fig. 2(a), the minimum temperature for austenite to form, Ac_1, is 700 °C and temperature for full austenitization, Ac_3, is 722 °C. Comparing with the classical pure Fe–C phase diagram, a three-phase zone, consisting of ferrite (α), cementite (θ) and austenite (γ), is recognized. The temperatures for the lower limit and the upper limit of the three-phase zone are the Ac_1 and 716 °C respectively.

The Fe–C phase diagram in Fig. 2(b), with hydrostatic pressure of 1.8 GPa, is different from the one calculated under atmosphere pressure in Fig. 2(a). The most obvious difference is the shift of eutectoid carbon concentration from 0.71 wt% in Fig. 2(a) to 0.48 wt% in Fig. 2(b). The Ac_1 temperature is 943 K (670 °C) and Ac_3 is 1050 K (777 °C). Comparing with the diagram for atmospheric pressure in Fig. 2(a), the highest temperature for cementite to remain stable changes from 716 °C in Fig. 2(a) to 777 °C in Fig. 2(b) for the present composition. The shift in the eutectoid composition indicates that if hydrostatic pressure during wheel/rail contact is high enough, the rail composition shifted from (near) eutectoid to hypereutectoid and cementite will be stable in a wider temperature range under high hydrostatic pressure.

3.2. Microstructures of simulated WEL and the rail WEL

Fig. 3(a) shows an optical image of the rail WEL. The specimen was cut cross-sectional so that the trains travelled perpendicular to the observed plane. After etching with 2% Nital, rail WEL is revealed as featureless white islands, separated by distinct boundaries from the brownish etched pearlite matrix. Some pearlite colonies are also etched white but can be easily identified by hardness measurements. The average thickness of the rail WEL is ~25 μm and the microhardness varies between 725 HV and 1050 HV. Immediately beneath the rail WEL, pearlite colonies appear intact and no flattening is recognized. The microhardness measurements in the pearlitic area under the rail WEL are close to the measurements in the original rail centre, indicating absence of work hardening.

Fig. 3(b) shows the microstructures, with mixed white and brown contrast under light reflection, in specimen $S_{730-020}$. The hardness of the brown region is ~290 HV, which is equivalent to the measured hardness of the central pearlite area in the studied

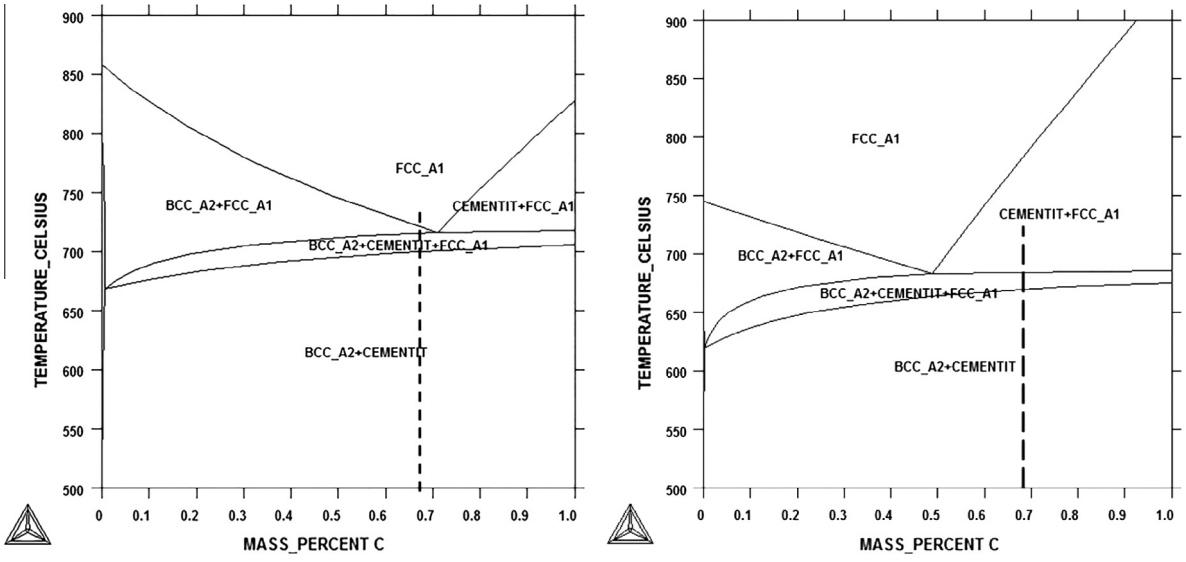

Fig. 2. Equilibrium quasi-binary iron-carbon phase diagram: (a) under atmospheric pressure, (b) under hydrostatic pressure of 1.8 GPa.

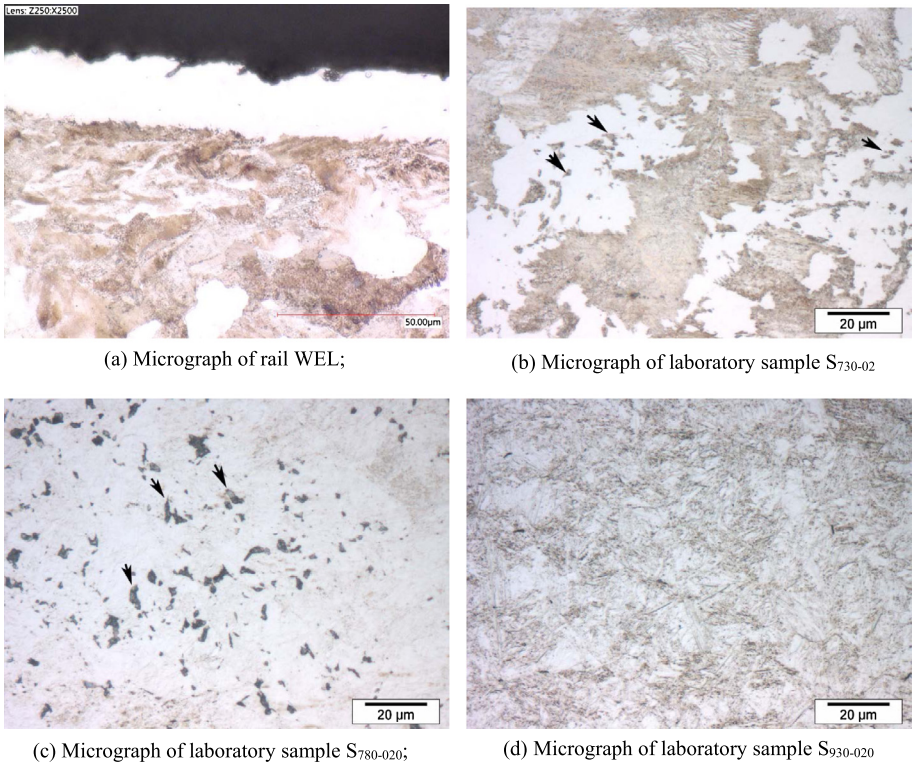

(a) Micrograph of rail WEL; (b) Micrograph of laboratory sample $S_{730\text{-}02}$

(c) Micrograph of laboratory sample $S_{780\text{-}020}$; (d) Micrograph of laboratory sample $S_{930\text{-}020}$

Fig. 3. Optical micrographs of: (a) rail WEL, and laboratory simulated specimen (b) $S_{730\text{–}020}$, (c) $S_{780\text{–}020}$ and (d) $S_{930\text{–}020}$. The arrows in (b) and (c) show untransformed pearlite within the martensite blocks.

rail section. The white area in Fig. 3(b) appears featureless for magnification up to 1000× and is much harder, 670–810 HV, than the brown pearlitic area. The hardness of the white zone compares well with the hardness of martensite with the carbon content of ~0.67 wt% for the studied rail [5]. Accordingly, the hard white phase is considered to be martensite. In addition, within the white martensite blocks, some brownish regions can be observed, c.f. indicated by arrows in Fig. 3(b). These regions are also identified as pearlite using SEM at higher magnification, see for example Fig. 4(c) in the later section. Martensite formed in the other specimens, e.g. $S_{780\text{–}020}$ in Fig. 3(c) or $S_{930\text{–}020}$ in Fig. 3(d), appears grey and is unlike the white martensite in Fig. 3(b). The mixed microstructure of martensite and pearlite is formed for austenitizing temperatures up to 830 °C, with reducing fraction of untransformed pearlite. Microstructures of samples $S_{880\text{–}020}$ and $S_{930\text{–}020}$ are similar and one example of microstructure of the sample $S_{930\text{–}020}$ is shown in Fig. 3(d). A single phase is observed, which is identified as martensite by means of hardness. Part of the martensite formed at these temperatures seems to have a needle-like shape. The grey particles in Fig. 3(d) are MnS inclusions, see our previous work [11]. Similar microstructures are observed in samples heated with 200 °C/s. The fraction of martensite, formed at temperatures of 730–830 °C with heating rate of 200 °C/s, is lower than those formed at heating rate of 20 °C/s.

Both the lab simulated and field rail specimens were characterized by SEM. Fig. 4(a) shows the SEM micrograph of an area inside the rail WEL and at a micrograph taken at WEL/pearlite boundary is shown in Fig. 4(b). Two types of lamellar features in the rail WEL can be observed: (i) the lamellar with multidirectional morphology, Fig. 4(a); (ii) line lamellar with aligned-like features, as indicated by arrows in Fig. 4(b). The aligned morphology is more obvious in areas close to the rail WEL/matrix boundary in Fig. 4 (b). Across the boundary, connection between cementite lamellae in pearlite and the aligned lamellae in the rail WEL are observed. Thus, the aligned lamellae in the WEL in Fig. 4(b) probably correspond to the previous locations of cementite. The distance between the aligned lamellae in rail WEL is similar to the cementite interlamellar distance in the adjacent pearlite. Occasionally, small isolated pearlite islands can be observed within the WEL, indicated by the open rectangle in Fig. 4(b).

Similar lamellar features are also observed in the laboratory formed WEL. Fig. 4(c) and (d) show SEM micrographs of laboratory specimen $S_{730\text{–}020}$. The dark grey zones in Fig. 4(c) and (d) are the martensite with no typical needle shape, as expected for a carbon concentration of 0.67 wt% in the studied rail steel. The similar lamellar features in Fig. 4(a) and (b) is recognized in Fig. 4 (c) and (d), in the laboratory specimen $S_{730\text{–}020}$. The aligned line lamellae in the martensite in Fig. 4(d) also appear to continue from the adjacent lamellar cementite in the pearlite matrix. The distance of aligned line morphology in the martensite appears the same as the adjacent cementite. Some untransformed pearlite within martensite block, corresponding to the brownish areas in the white martensite block in Fig. 3(b), is recognized in Fig. 4(c). It is observed that the martensite formed in specimens heated to 780 °C and higher temperatures has the lath-like morphology and is significantly different from the rail WEL. As a result, the microstructures in specimens heated to 780 °C and higher temperatures will not be shown and discussed.

Fig. 5(a) and (b) show the SEM images of the rail WEL and simulated WEL in specimen $S_{730\text{–}200}$ respectively. The dashed lines in Fig. 5(a) schematically indicate the WEL/pearlite boundaries. Fig. 5(b) and (c) are grey scale image quality (IQ) maps, imposed by the map of austenite phase, in red, of Fig. 5(a) and (b) respectively. Both WELs appear darker than the pearlite matrix in the IQ maps, probably due to the dislocation density in the WELs. The white lines in Fig. 5(c) delineate the axis/angle rotation of 90° ⟨1 1 2⟩, representing the Kurdjumov–Sachs (K–S) orientations between martensite and austenite. The match of K–S orientation

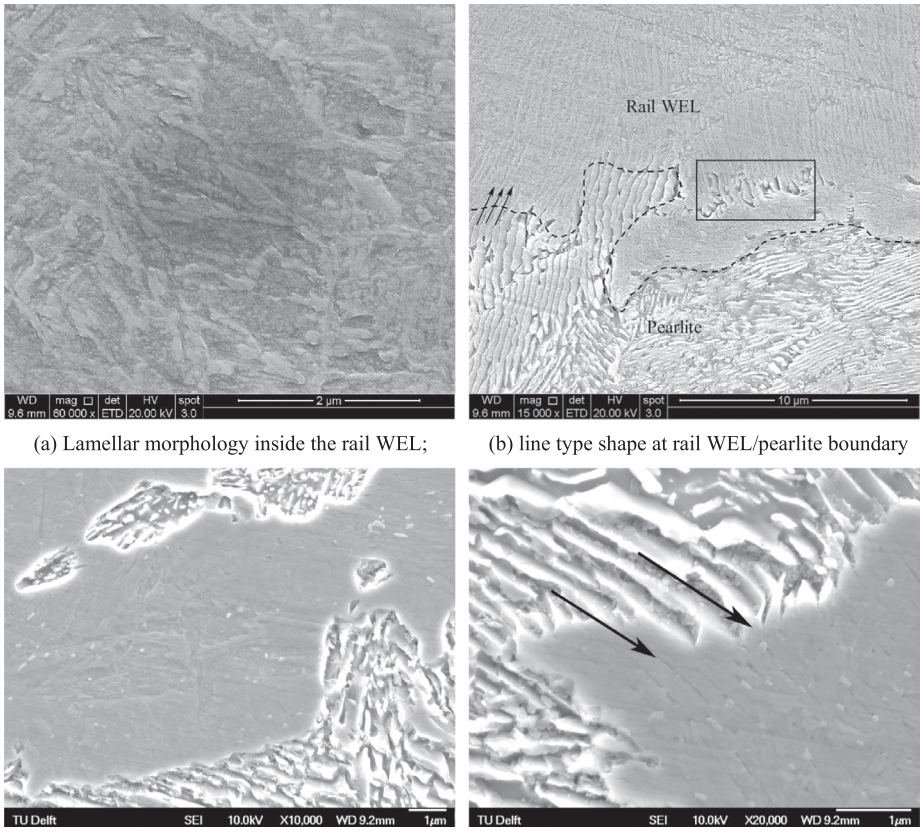

(a) Lamellar morphology inside the rail WEL; (b) line type shape at rail WEL/pearlite boundary

(c) Lamellar features in the laboratory sample $S_{730\text{-}020}$; (d) line type features in laboratory sample $S_{730\text{-}020}$.

Fig. 4. SEM micrographs showing: (a) lamellar morphology in the rail WEL, (b) the aligned line feature at the rail WEL/pearlite boundaries, (c) lamellar morphology and (d) line feature in in laboratory specimen $S_{730\text{–}020}$. The dashed line in (b) decorates the rail WEL/pearlite boundary and the arrows in (b) and (d) indicate the continuation from cementite lamellar in pearlite to line feature in rail WEL and laboratory WEL. Note the difference of scales.

between austenite and ferrite, in Fig. 5(c), strongly supports the martensitic nature of the rail WEL. Austenite is also identified in the laboratory WEL in Fig. 5(d).

A plot of the grain diameter vs. the number fraction of the grains in the rail WEL and the laboratory simulated WEL in specimen $S_{730\text{–}200}$, is shown in Fig. 5(e). To build this plot, only the WELs are cropped and the pearlitic zones are discarded for the quantitative comparison. It can be seen that the grain size range in the rail WEL and the laboratory WEL in $S_{730\text{–}200}$ is comparable. There are higher fractions of grains, smaller than 300 nm, in the rail WEL than those in $S_{730\text{–}200}$, Fig. 5(e). This is probably due to the grain refinement in the rail WEL by the deformation, exerted by the passing trains. It should also be noticed that the maximum grain diameter in rail WEL, 3.62 µm, is also larger than that in the simulated WEL in $S_{700\text{–}200}$, 1.66 µm. The average grain size measured in the rail WEL, Fig. 5(c), is 272 nm whereas the average grain size of the laboratory WEL in Fig. 5(d) is 269 nm.

Kernel average orientation (KAM) maps are often used to evaluate the strain distribution and they link the local lattice distortion measured via EBSD to the dislocation density in the material [14]. The KAM plot of the rail WEL and the laboratory WEL is shown in Fig. 5(f). The analysis shows that the martensitic structure formed in the rail WEL has higher KAM than the one formed via lab simulation. This observation is logically consistent with the fact that the martensite in the WEL in rails is formed in the conditions of severe local deformation. Such conditions do not exist during the lab simulations of WEL.

4. Discussion

4.1. Comparison to the literature on rail WELs

A comparison of the characteristics of the studied rail WEL with WELs in literature will be first made. Due to the widely reported nanometre scale microstructure of WEL in rails, high resolution techniques are usually required, such as using TEM or synchrotron XRD as summarized in Table 1. For example, lattice tetragonality detected by synchrotron XRD is convincing evidence for the martensite nature of the WEL, e.g. [5,8]. In some cases, micro mechanical property measurements, e.g. by hardness tests, can be useful in differentiating WELs formed by different mechanisms. For example, the nanocrystalline ferrite rail WEL is commonly reported to be accompanied by the following features in the adjacent pearlite [9,10]: (i) a transient work-hardened pearlite zone beneath the WEL, (ii) an obvious reduction of the interlamellar cementite distance in the work-hardened pearlite zone. Consequently, observations of absence of work-hardened zone and the cementite lamellae thinning in the pearlite matrix, e.g. [7], can be a strong indication of WEL not being formed by severe plastic deformation. Consequently, the studied rail WEL is most probably martensite due to the observation of: (i) the almost intact pearlite colonies immediately beneath WEL in the rail sample, Fig. 3(a), and the absence of work-hardened pearlite area beneath WEL; (ii) the almost unchanged interlamellar distance within the WEL, compared with the one in the connecting matrix, c.f. Fig. 4(b); (iii) The identification of retained austenite in the rail WEL in Fig. 5(c).

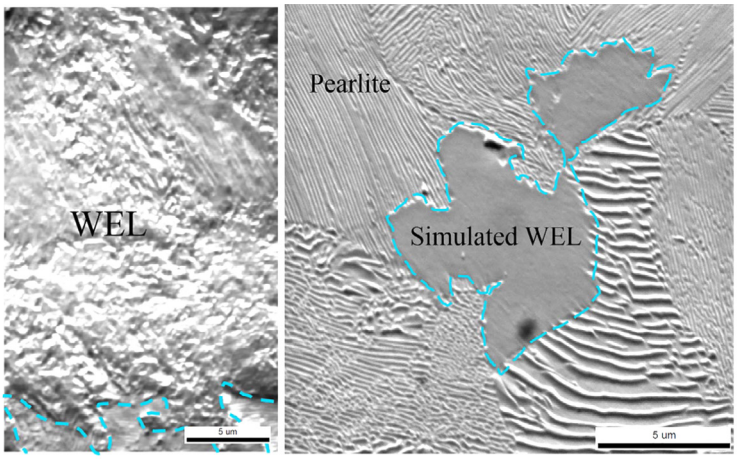

(a) SEM micrograph of rail WEL; (b) SEM micrograph of simulated WEL in sample $S_{730\text{-}200}$

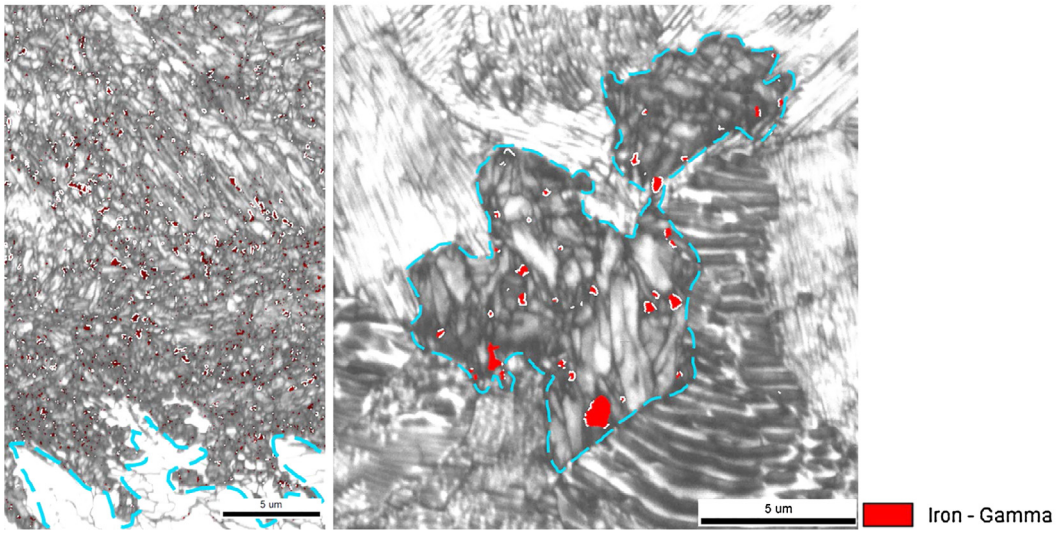

(c) IQ and austenite map of rail WEL; (d) IQ and austenite map of simulated WEL in sample $S_{730\text{-}200}$

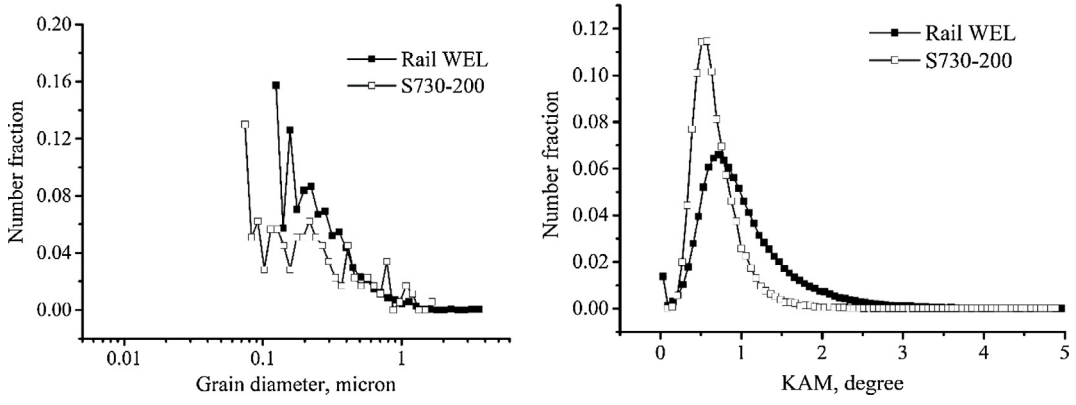

(e) Plot of grain diameter distribution in rail WEL and simulated WEL; (f) KAM plot of rail WEL and simulated WEL

Fig. 5. (a) SEM micrograph of rail WEL. The blue lines indicate the WEL/pearlite boundary; (b) the SEM micrograph of the simulate WEL in sample $S_{730-200}$; (c) the IQ map of rail WEL in (a), imposed with austenite phase map. The phase boundaries satisfying the K–S orientation relationship are delineated by the white lines; (d) the IQ map of laboratory WEL of specimen $S_{730-200}$ in (b), imposed with austenite phase map; (e) grain diameter distribution of both rail WEL and laboratory WEL in $S_{730-200}$; (f) KAM distribution of both rail WEL and laboratory WEL in $S_{730-200}$. (For interpretation of the references to colour in this figure legend, the reader is referred to the web version of this article.)

The laboratory simulated WEL consists of martensite with a similar morphology as observed in the studied rail WEL, see Fig. 4(a)–(d). The hardness of the simulated WEL, corresponding to Fig. 4(c) and (d), is 670–810 HV. This is in general a bit lower than the measurements in the rail WEL, 725–1050 HV. However, the current laboratory tests represent only one phase transformation cycle. Five repeated heat treatment cycles have been done to specimen $S_{730-200}$ and the hardness increases to 700–850 HV. Repeated fast heat treatments form a well-known procedure for producing finer martensite, thus higher hardness, c.f. [15]. Accordingly, martensite with equivalent hardness as the rail WEL might be produced after multiple wheel passages. In addition, the well-controlled heat treatment also allows relating the quantitative microstructure analysis to the exact heat treatment. The microstructural quantification from experimental simulation can be used to clarify rail WEL formation due to increased temperature, in condition where the heating rate is much higher than the current laboratory work.

The temperature change during wheel/rail contact appears to play an important role in arguing the WEL formation mechanisms. For example, Newcomb [9] characterized the WEL to be fully martensitic. However, the martensite transformation theory is not supported by the temperature rise calculation. As an alternative, he proposes that the martensite in the WEL is a ferrite with supersaturated carbon, which is accommodated by dislocations generated due to plastic deformation.

In the following sections, the temperature rise in the studied rail will be estimated using finite element modelling (FEM). A subsequent discussion on the observed microstructures in the laboratory simulated WEL and the rail WEL will also be made.

4.2. Estimation of temperature rise using FE method

When wheels are running on rails, the frictional heat is generated at the wheel/rail contact interfaces, causing temperature rise in the materials. The thermo-mechanical behaviour of the wheel–rail contact has been widely studied in the literature, see e.g. [16,17]. The problem of the temperature rise in the wheel–rail system has recently been investigated, using a coupled thermal–mechanical analysis [18]. With the finite element (FE) tool developed in [18], the frictional heat generated during rolling contact and the resulting temperature rise in the materials can be calculated.

The model used for the current calculation is shown in Fig. 6. The wheel and rail materials are assumed to behave elastically and they are meshed with 8-node solid elements. To achieve high accuracy with reasonable computing time, non-uniform mesh is applied with the finest element size of $0.3 \times 0.3\ mm^2$ in the solution zone. At the beginning of the simulations, the materials are uniformly at the ambient temperature and the thermo-mechanical stresses are zero. The magnitudes of the stresses and the temperature at a material point at the contact interface ascend when the wheel approaches it. Four points were selected at the nodes shown in Fig. 6 for the temperature output. Using the parameters listed in Table 2, a wheel with a typical velocity of 140 km/h of the Dutch trains rolling along a straight rail was considered with a longitudinal creepage of 3.6%. This corresponds to a slip velocity of 5 km/h. A high friction coefficient of 0.6 was used and the ambient temperature was set to 25 °C. This choice is made, since a higher friction induces greater heat generation at the contact interface, leading to a more critical state. A higher magnitude of creepage can also lead to higher temperature rise. It is in practice, however, unlikely to have very high creepage in the presence of a high friction coefficient. With a creepage of 3.6% and a friction coefficient of 0.6, the contact was around the point of full slip, i.e. loss of adhesion area in the contact patch, while the wheel was rolling. This is thus indeed a critical situation. According to [9], this status of the friction and creepage was roughly estimated to generate a flash temperature of around 700 °C.

The temperature evolution with time in the rail surface was calculated and shown for the four nodes, Fig. 7(a), and their average, Fig. 7(b). The nodes were in the middle of the running band, where maximum temperature rise is expected. The temperature increases abruptly when the wheel arrives at the nodes. The peak temperature is obtained, when the nodes are in the rear part of the contact. When the wheel leaves the nodes, they rapidly cool down.

The highest temperature occurred at node 1 with 730 °C. This temperature is higher than both the Ac_1 for steel under atmosphere pressure, which is 700 °C (cf. Fig. 2(a)) and the Ac_1 of steel under hydrostatic pressure of 1.8 GPa, which is 670 °C, (cf. Fig. 2(b)). The average maximum temperature of the four nodes is 670 °C. It is 30 °C lower than the Ac_1 for steel under atmosphere pressure (700 °C), but it is the same as Ac_1 of steel under hydrostatic pressure of 1.8 GPa, (670 °C). Hence, it is possible that the heat generation in the wheel/rail contact increases the rail surface temperature above the critical one for austenite formation.

Using the data plotted in Fig. 7(b), one can estimate the average heating and cooling rate in the rail during wheel passage. The average heating rate is estimated to be 1.5×10^6 °C/s. The cooling rate between 700 °C and 400 °C, which is the temperature zone for pearlite and bainite formation, is estimated to be 1.7×10^6 °C/s. This cooling rate should be sufficient to prohibit the formation of pearlite or bainite. The cooling rate between 300 °C and 46 °C, within which martensite transformation is expected for the

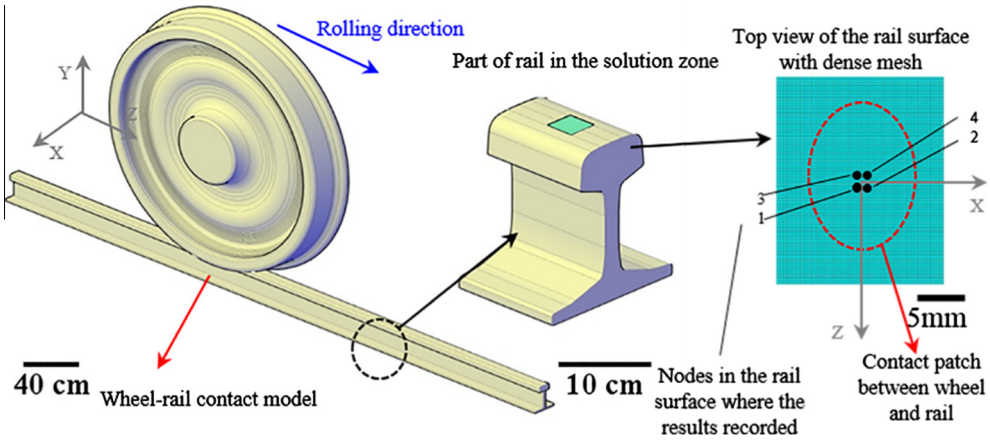

Fig. 6. The wheel–rail contact model for calculating temperature rise due to frictional heat.

Table 2
Parameters used in the thermo-mechanical FE model for typical critical Dutch-operation conditions.

Symbol (units)	Description	Values
V (km/h)	Wheel forward velocity	140
S (%)	Creepage	3.6
V_s (km/h)	Slip velocity	5.0
f	Coefficient of friction	0.6
E (GPa)	Young's modulus	210
υ	Poisson's ratio	0.3
κ (m^2/s)	Thermal diffusivity	1.518×10^{-5}
λ (W/°Cm)	Thermal conductivity	50
ρ (kg/m^3)	Density	7850
c (J/kg/°C)	Specific heat capacity	419.5
N (kN)	Normal load	134
M_w (kg)	Wheel weight	900
R_w (m)	Wheel radius	0.46
T_0 (°C)	Ambient temperature	25

studied rail composition, is around 3.9×10^4 °C/s. Martensite can then form when the surface is cooled to the ambient temperature.

4.3. Thermodynamic interpretation

The observed microstructures in the laboratory specimens can be interpreted from thermodynamic and kinetic theories. As discussed in the previous section, a mixture of martensite and pearlite is identified in laboratory specimens $S_{730-020}$ till $S_{830-020}$, using hardness measurements and SEM. This means that the initial pearlite has partially transformed to austenite and martensite forms because of the subsequent fast quenching during the laboratory experiments. When a specimen was heated to temperature of 880 °C and higher, cementite was not observed and a possible single martensite is detected by hardness measurements, Fig. 3(d). Comparing with the calculated Fe–C phase diagram in Fig. 2(a), the specimens with mixed martensite and pearlite microstructure must have been heated to the temperatures within the three-phase region in Fig. 2(a). For temperatures above the three-phase region, no cementite is expected.

The theory of phase transformation kinetics should be applied for the interpretation. The changes of the upper limit temperature can be the result of a local non-equilibrium condition due to the fast heating [19]. The equilibrium carbon concentration in austenite formed in the three-phase region is calculated with Thermo-Calc to be nearly constant as 0.69 wt%. As a result, carbon partitioning is needed for austenite to form, through a diffusional process. Carbon diffusion from cementite to the austenite/ferrite phase front is required for austenite to grow. The increasing heating rate shortens the diffusion time, thus the diffusion distance, of carbon in austenite for the same austenitizing temperature. As a result, the complete transformation of cementite to austenite will be delayed, leading to the observation of lamellae or the line traces in martensite, c.f. Fig. 4(d). This also matches well with the observed less amount of martensite formed in heat treatment with higher heating rate.

Similar arguments can also be used to interpret the observed microstructure of the studied rail WEL. As discussed in the previous sections, the studied rail WEL is probably martensite on the basis of comparison with the literature and comparison with the laboratory simulate WEL. The temperature calculations also support the WEL formation through martensite phase transformation in the studied rails. As a result, the rail WEL forms most probably due to phase transformation and the interpretation for the observed microstructure in the laboratory specimens can also be used for the observations in rail WEL.

For the diffusional transformation of pearlite to austenite, the diffusion of alloying elements in austenite determines the growth kinetics of austenite. Therefore, an estimation of diffusion distance of alloying elements will be made. According to the current FEM simulation, the rail surface is unlikely to be heated up to 900 °C or higher, below which the diffusivity of manganese and silicon in the austenite is low [20]. Therefore, only carbon diffusion will be evaluated and only the diffusion distance of carbon in the austenite will be estimated. The diffusivity, D, of carbon in austenite is expressed as:

$$D = D_0 \times exp^{-\frac{Q}{RT}}, \tag{1}$$

where $D_0 = 0.234 \times 10^{-4}$ m^2/s, is the pre-coefficient, $Q = 147.81$ kJ/mol is the activation energy, R is the gas constant, T is the temperature at which the interstitial element diffuses [21].

The average diffusion distance, L, is then approximated by

$$L = \sqrt{Dt}, \tag{2}$$

where t is the diffusion time within the austenitizing temperature zone which is calculated by:

$$t = \frac{(T - T_{Ac1})}{v} \tag{3}$$

where T_{Ac1} is the A_{c1} temperature and v is the heating rate.

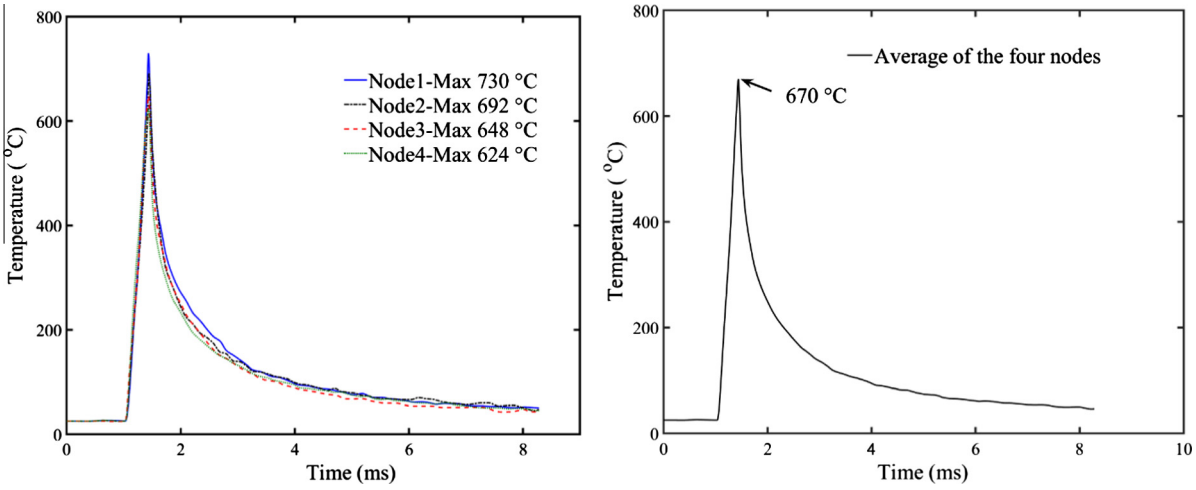

Fig. 7. (a) The temperature evolution with time in the rail surface of the four nodes in Fig. 6; (b) the average temperature variation with time of the four nodes.

It has been shown that the hydrostatic pressure of 1.8 GPa only leads to minor reduction in A_{c1}, 30 °C, from the one calculated at atmospheric pressure. The equilibrium A_{c1} of atmospheric pressure will be used for calculating the diffusing time, t. Since carbon can diffuse into ferrite from the two neighbouring cementite plates for a lamellar pearlite microstructure the maximum diffusion distance for the carbon from cementite to ferrite then equals half the cementite interlamellar distance, namely 75 nm. Using Eqs. (1)–(3), a maximum temperature of 1034 °C is required for carbon to diffuse for such distance in one single heating cycle using the heating rate of 1.7×10^6 °C/s, estimated from previous FEM simulation. This temperature is much higher than the calculated temperature in Fig. 7(a) and (b). At lower temperature, the diffusivity D and diffusion t reduce, leading to shorter diffusion distance. It is thus can be speculated that multiple cycles will be needed for the pearlite to be fully austenitized.

The hydrostatic pressure of 1.8 GPa also leads to a shift of the eutectoid point, from 0.7 wt%C under atmosphere pressure to 0.48 wt%C, cf. Fig. 2(a) and (b). This means that during the wheel/rail contact, the rail composition will become hypereutectoid, if the generated hydrostatic pressure is high enough. This will cause the cementite to be stable at higher temperature than for an hypo-eutectoid composition. After load releases, the rail composition returns to be hypo-eutectoid and the microstructure is expected to consist of martensite and cementite. As a consequence, detection of cementite in the martensite WEL, c.f. [5], can be either due to the shift of eutectoid point due to external load or due to the pearlite being heated to the three-phase region in the phase diagram in Fig. 2(a).

It is shown in this study that WEL formation through martensite phase transformation is supported by laboratory simulations, numerical temperature simulations and thermodynamic calculations. However, in our simulations only temperature effect is simulated while the contact pressure from the train passage is only estimated but not simulated. Further work should be done to clarify the hypothesis: (i) clarification of the microstructural nature of the observed WEL in rail must be characterized by higher-resolution techniques, such as transmission Kikuchi diffraction (TKD), TEM or APT. (ii) loads must be considered together with the temperature to make the simulation close to the real situation. The higher KAM in the rail WEL than in the laboratory WEL in $S_{730-200}$, Fig. 5(f), indicates the deformation history in the rail WEL. Simultaneous deformation and temperature increase generate the martensitic microstructure with similar morphology as the one generated in laboratory simulation but probably with higher density of the crystal lattice defects, like geometrically necessary dislocations (GNDs). It is also reported that the severe plastic deformation can lead to dissolution of cementite. Ferrite with supersaturated carbon, e.g. trapped in dislocations, will reduce the temperature of α to γ phase transformation, possibly even to room temperature [22].

5. Conclusions

Martensitic WEL is simulated in the laboratory by fast heat treatments, using heating rates of 20 °C/s and 200 °C/s. Characteristics of the transformed martensite are analyzed by microhardness, optical microscopy, scanning electron microscopy and electron backscatter diffraction. Microstructures of WEL from the studied rail surface are also investigated and compared with the microstructures of simulated martensite. The main results can be summarized as follows:

1. Rail WEL is martensite.
2. White etching areas form in the laboratory simulations.
3. Mixed microstructures of martensite and pearlite are both identified in samples heated to temperatures of 730–830 °C. This can be interpreted by the deviation from equilibrium condition in the three phase region of ferrite, cementite and austenite in the calculated iron–carbon phase diagram due to fast heating rates.
4. Hydrostatic pressure of 1.8 GPa leads a 30 °C reduction in the austenite start temperature and a significant shift of the eutectoid carbon concentration. Due to high external pressure the eutectoid carbon concentration shifts from 0.7 wt%C to 0.48 wt%C and the corresponding A_1 temperature changes from 700 °C to 670 °C.
5. On the basis of comparison with the observed WEL in rails and the simulated WEL and WEL from literature, it is shown that the investigated WEL in rail is most likely to be martensite. The observations find good support by the thermodynamic and kinetic simulations and numerical frictional heat simulation.

Acknowledgements

STW-the Dutch Technology Foundations and ProRail are acknowledged for the financial support in the frame of the project PRIME (High Performance Rail through Intelligent Metallurgy & Engineering). ProRail is acknowledged for supporting the research with providing the material and data for the study.

References

[1] Dikshit V, Clayton P, Christensen D. Investigation of rolling contact fatigue in a head-hardened rail. Wear 1991;144:89–102. http://dx.doi.org/10.1016/0043-1648(91)90008-I.
[2] Steenbergen M, Dollevoet R. On the mechanism of squat formation on train rails – Part I: origination. Int J Fatigue 2013;47:361–72. http://dx.doi.org/10.1016/j.ijfatigue.2012.04.023.
[3] Clayton P, Allery MBP. Metallurgical aspects of surface damage problems in rails. Can Metall Q 1982;21:31–46. http://dx.doi.org/10.1179/cmq.1982.21.1.31.
[4] Lojkowski Djahanbakhsh M, Bürkle G, Gierlotka S, Zielinski W, Fecht HJW. Nanostructure formation on the surface of railway tracks. Mater Sci Eng A 2001;303:197–208. http://dx.doi.org/10.1016/S0921-5093(00)01947-X.
[5] Österle Rooch H, Pyzalla A, Wang LW. Investigation of white etching layers on rails by optical microscopy, electron microscopy, X-ray and synchrotron X-ray diffraction. Mater Sci Eng A 2001;303:150–7. http://dx.doi.org/10.1016/S0921-5093(00)01842-6.
[6] Zhang HW, Ohsaki S, Mitao S, Ohnuma M, Hono K. Microstructural investigation of white etching layer on pearlite steel rail. Mater Sci Eng A 2006;421:191–9. http://dx.doi.org/10.1016/j.msea.2006.01.033.
[7] Takahashi J, Kawakami K, Ueda M. Atom probe tomography analysis of the white etching layer in a rail track surface. Acta Mater 2010;58:3602–12. http://dx.doi.org/10.1016/j.actamat.2010.02.030.
[8] Wang Pyzalla A, Stadlbauer W, Werner EAL. Microstructure features on rolling surfaces of railway rails subjected to heavy loading. Mater Sci Eng A 2003;359:31–43. http://dx.doi.org/10.1016/S0921-5093(03)00327-7.
[9] Newcomb SB, Stobbs WM. A transmission electron microscopy study of the white-etching layer on a rail head. Mater Sci Eng 1984;66:195–204. http://dx.doi.org/10.1016/0025-5416(84)90180-0.
[10] Baumann G, Fecht HJ, Liebelt S. Formation of white-etching layers on rail treads. Wear 1996;191:133–40. http://dx.doi.org/10.1016/0043-1648(95)06733-7.
[11] Wu J, Petrov RH, Naeimi M, Li Z, Sietsma J. A Microstructural Study of Rolling Contact Fatigue in Rails. In: Proc Second Int Conf Railw Technol Res Dev Maintenance, Ajaccio. Civil-Comp Press; 2014. Fr. 8–11 April.
[12] Rovira A, Roda A, Marshall MB, Brunskill H, Lewis R. Experimental and numerical modelling of wheel–rail contact and wear. Wear 2011;271:911–24. http://dx.doi.org/10.1016/j.wear.2011.03.024.
[13] Porter DA, Easterling KE, Sherif M. Phase transformations in metals and alloys, (Revised Reprint). CRC Press; 2009.
[14] Wright SI, Nowell MM, Field DP. A review of strain analysis using electron backscatter diffraction. Microsc Microanal 2011;17:316–29. http://dx.doi.org/10.1017/S1431927611000055.
[15] Tsuji N, Maki T. Enhanced structural refinement by combining phase transformation and plastic deformation in steels. Scr Mater 2009;60:1044–9. http://dx.doi.org/10.1016/j.scriptamat.2009.02.028.
[16] Fischer FD, Werner E, Yan W-Y. Thermal stresses for frictional contact in wheel–rail systems. Wear 1997;211:156–63. http://dx.doi.org/10.1016/S0043-1648(97)00108-7.

[17] Ertz M, Knothe K. Thermal stresses and shakedown in wheel/rail contact. Arch Appl Mech 2003;72:715–29. http://dx.doi.org/10.1007/s00419-002-0255-4.
[18] Naeimi M. Computation of the flash-temperature at the wheel–rail contact using a 3D finite element model and its comparison with analytical methods. In: 10th Int Conf Contact Mech. (CM 2015); 2015.
[19] Meshkov YY, Pereloma EV. 17 – The effect of heating rate on reverse transformations in steels and Fe–Ni-based alloys. In: Pereloma E, Edmonds DV, editors. Phase Transform Steels, vol. 1. Woodhead Publishing; 2012. p. 581–618. http://dx.doi.org/10.1533/9780857096104.4.581.
[20] Savran VI. Austenite formation in C-Mn steel. TU Delft: Delft University of Technology; 2009.
[21] Mehrer Wever HH, editor. Landolt-Bornstein. Numerical data and functional relationships in science and technology, new series, group III: crystal and solid state physics: diffusion in metals and alloys, vol. 26. Berlin: Springer-Verlag; 1990. ISBN 3-540-50886-4 [Berichte Der Bunsengesellschaft Für Phys Chemie 1993;97:952. http://dx.doi.org/10.1002/bbpc.19930970725].
[22] Min N, Li W, Jin X. α to γ transformation in the nanostructured surface layer of pearlitic steels near room temperature. Scr Mater 2008;59:806–9. http://dx.doi.org/10.1016/j.scriptamat.2008.05.038.